Derivation and Validation of Three-dimensional Microwave Imaging Using a W-band MIMO Radar

Sumin Kim, *Student Member, IEEE,* Jeongbae Kim, *Student Member, IEEE,* Chaerin Chung, *Student Member, IEEE,* Min-Ho Ka, *Member, IEEE,*

***Abstract*—This study proposes a method for synthesizing three-dimensional (3-D) microwave images using a multiple-input multiple-output (MIMO) radar. Recent studies on MIMO radar technology have reported promising hardware that can be used in radar imaging. Particularly, the increased amount of data acquired from MIMO radar is effective for 3-D radar imaging. Despite the demand for using 3-D radar imaging the underlying technical challenges have not been addressed. Although the array synthetic aperture radar method is promising, realizing a multichannel radar with numerous channels requires significant effort in terms of hardware. Therefore, a MIMO radar can be used to effectively increase the number of channels with reduced hardware. Studies on beat frequency division (BFD) FMCW radars show that the simultaneously transmitted MIMO signal is suitable for radar imaging applications without hindering the along-track imaging performances. In this study, the signal of a BFD FMCW radar mounted on a movable platform is modeled according to the imaging geometry, and a fast Fourier transform-based imaging algorithm is derived to efficiently process the multichannel data. This algorithm is applied to the simulated radar data to verify the effectiveness of the proposed method. The method is further assessed by applying the imaging algorithm to the radar data acquired from a functional W-band BFD FMCW radar hardware. The radar transceiver was mounted on a movable table, and the data are measured at an outdoor experiment site. The results verify that the proposed method can be used for various 3-D radar imaging applications.**

***Index Terms*—radar imaging, W-band, three-dimensional imaging, MIMO radar**

I. Introduction

RECENT advances in the multiple-input multiple-output (MIMO) radar technology report that a multichannel radar with numerous channels can be realized with reduced hardware. Jeon et al. successfully demonstrated the generation of a radar image using sufficiently small MIMO radar that can be mounted on a movable platform [1], [2]. Although the applications of MIMO technology have been thoroughly investigated, increasing the number of radar channels can be highly effective for three-dimensional (3-D) microwave imaging [3], [4].

3-D radar systems and algorithms are increasingly investigated owing to the improvements in radar technology and radar imaging algorithms [5]. In conventional two-dimensional radar imaging systems, 3-D distributed scene reflectivity is projected onto a plane containing the line-of-sight (LOS) and along-track directions [6]. However, the backscattering information along the cross-track direction is lost in the process. The radar 3-D imaging technology attempts to preserve the aforementioned information to be used in complex surveillance challenges, target recognition, and tomographic mapping [7].

Radar data acquisition of a conventional 2-D imaging system can be performed using different points on a line. However, additional data measurements and processing are required to preserve the backscattering information along the elevation direction. The existing 3-D radar imaging methods include tomographic synthetic aperture radar (tomoSAR), circular SAR (CSAR), and array SAR.

In the tomoSAR method, multiple radar data acquired from different heights are processed to generate a 3-D radar image [8], [9], [10], [11], [12], [13]. Reigber and Moreira demonstrated the feasibility of the tomoSAR method by acquiring multiple radar datasets from a series of airborne SAR measurements [8]. The tomographically processed data exhibited volumetric scattering of the target scenes, including an illuminated forest, and the height of a building from the ground. Subsequently, Huang et al. extended the approach to detect concealed objects under a forest canopy using a wavelet-based tomography estimation method [9].

The application of the the tomoSAR method in 3-D radar imaging using a single channel system requires multiple radar measurements of the target scene. However, performing these measurements may be expensive and time-consuming, which is unfavorable for applications such as urgent surveillance missions.

Conversely, the CSAR method can synthesize a 3-D radar image using a single radar measurement [14], [15], [16], [17], [18]. In this method, points on a circular track centered at the region of interest are used to acquire radar data. Ponce et al. used the data acquired from a circular track to synthesize the 3-D imaging of a tree based on radar polarimetry [14]. However, the performance of the 3-D radar image using single-pass CSAR data was insufficient owing to the cone-shaped sidelobes which led to developments in tomographic CSAR methods [15], [16]. Nevertheless, combining the CSAR and tomoSAR methods shares the aforementioned disadvantages of the tomoSAR method.

Therefore, array SAR involving the radar data collection from a multichannel radar is gaining attention. In the array SAR method, multiple antennas arranged in the cross-track direction are used to acquire the radar data when the radar platform travels in the along track direction. Additionally, a method to obtain radar data using an antenna array distributed

The authors are with the School of Integrated Technology, Yonsei University, Incheon, 21983 Republic of Korea, e-mail: kaminho@yonsei.ac.kr

Manuscript received November 01, 2020; revised August xx, xxxx.

This work was supported by the National Research Foundation of Korea (NRF) grant funded by the Korea government (MSIT) (2021R1A2C2006025)

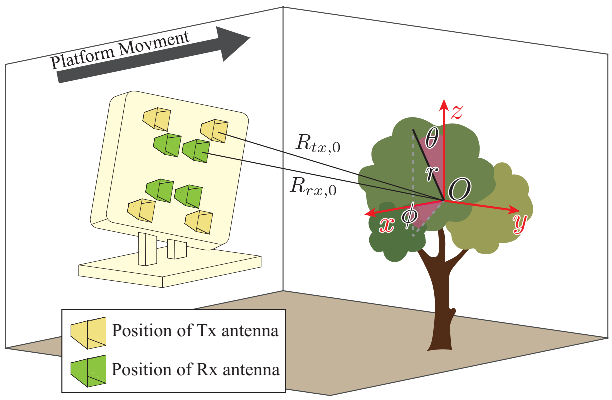

Fig. 1. Imaging geometry of the proposed three-dimensional (3-D) radar imaging method showing a multiple-input multiple-output (MIMO) radar moving in the along-track direction.

along the wingspan of an aircraft illuminating the ground has been thoroughly investigated for practical applications of winged airplanes [19], [20], [21], [22], [23]. Zhang et al. proposed the process of radar data acquisition using the aforementioned method with fast Fourier transform multiple signal classification (FFT-MUSIC) to synthesize a 3-D radar image [21]. Single-channel radar data resembling the array SAR data were used to validate the proposed method. Recently, Kang et al. proposed improving the array SAR method for 3-D radar imaging by applying a super-resolution technique. Their method was validated by synthesizing a 3-D radar image using the data generated by a distributed target simulation [20].

To enhance the resolution of the 3-D radar image using the array SAR method, multiple radar antennas broadly distributed along the cross-track direction are required [19]. While the realization of a multichannel radar may warrant immense hardware effort, MIMO technology can aid in accomplishing the equivalent by orthogonal transmission and reception of radar signals.

MIMO radar can effectively increase the number of antennas with fewer physical elements [3]. By separating the individual transmit (Tx) channels from the receive (Rx) channel, data from $M \times N$ channels can be acquired using M Tx and N Rx channels. Typically, the Rx channels are separated using individual signal paths. Signal transmission from multiple Tx channels can be achieved using time division multiplexing (TDM) or frequency division multiplexing (FDM). However, simultaneous transmission of transmit signals is not possible using the TDM method, which decreases the effective pulse repetition frequency (PRF). According to the radar imaging principle, a high PRF is required to enhance the along-track resolution [5]. Therefore, an FDM scheme with simultaneous transmission capabilities is necessary to maintain the along-track imaging performance.

Presently, orthogonal frequency division modulated (OFDM) waveforms are being researched as a candidate for FDM MIMO imaging radars [20], [24], [25]. Nevertheless, imaging radar hardware utilizing the OFDM waveform has not been reported due to the sensitivity to Doppler shift.

The beat frequency division (BFD) frequency modulated continuous wave (FMCW) utilizes the FDM method to transmit multiple signals simultaneously [2], [26], [27], [28]. Feger et al. realized 6×8 BFD FMCW hardware and performed a stationary measurement of a target scene to synthesize a 2-D radar image [26]. Previously, we realized a small-sized BFD FMCW radar mounted on a movable platform. Imaging results indicated that simultaneously transmitted signals are suitable for radar imaging applications [2]. In this study, we synthesized a 3-D radar image by illuminating the target scene with MIMO hardware mounted on a mobile platform to advance our previous work.

Although the data acquired from MIMO radar provides an opportunity to synthesize a 3-D image, efficient and advanced radar imaging algorithms cannot be applied to multi-static measurement geometry. The backprojection algorithm that uses the positions of Tx and Rx antennas can be applied at the cost of a high computational load [29]. Rigling and Moses proposed a radar imaging algorithm applicable to bistatic radar configurations with separate Tx and Rx antennas [30]. According to them, the reduced computation of FFT can be exploited to synthesize a 2-D radar image from a bistatic radar measurement. In this study, the radar signal was modeled according to multi-static geometry to advance the aforementioned method. Consequently, a novel imaging algorithm that can synthesize a 3-D radar image using the data from a MIMO radar mounted on a movable platform was derived.

To validate the proposed method and imaging algorithm, simulated radar data were generated assuming that point scatterers are distributed in a volumetric space. The simulation parameters were referenced from the operational MIMO radar reported by Jeon et al., which utilizes a center frequency of 94 GHz for high-resolution radar imaging [1], [2]. The proposed algorithm was applied to the simulated data and the resultant 3-D imaging results were analyzed.

While the proposed method is not limited to a specific electromagnetic spectrum, it is especially effective for millimeter wave systems which are experiencing a spontaneous growth due to the increase in demands for automobiles and small-sized aircrafts [31], [32]. Mobile platforms with limited payload and size requires the radar system to be small-sized and light-weighted, which can easily be accomplished with systems utilizing a small wavelength. Moreover, a large ratio between the array size and the wavelength is preferred for the cross-track resolution performances, which can also be accomplished by the W-band system utilized in this paper.

Further validation was performed by applying the imaging algorithm to radar data acquired using the proposed method. To measure the MIMO radar signal, the hardware reported by Jeon et al. was mounted on a movable table. The platform was placed on smooth ground at Yonsei University, Republic of Korea, and the radar data were measured while moving the platform at a low speed. Triangular trihedral corner reflectors resembling simple point scatterers and a personal vehicle representing a complex structured object were used as targets for the experiments. The imaging results provided an accurate localization of the corner reflectors in the volumetric space, and those of the personal vehicle exhibited the detailed structure of the complex target. The experiment result shows that the proposed method is applicable to small-scale tomographic mapping and can retrieve the 3-D scattering information small targets.

The remainder of this paper is organized as follows. Section II introduces the 3-D imaging geometry of the proposed method and describes the signal model of the MIMO radar signal. An efficient imaging method that utilizes FFT was derived from the signal model. In Section III, the proposed method is validated by generating the simulated MIMO radar data and applying the imaging algorithm to the simulated data. Section IV explains the process of the radar data acquisition using MIMO radar hardware. Furthermore, the proposed method is validated by synthesizing a 3-D image of the illuminated targets. Section V summarizes the conclusions of the study.

II. 3-D Radar Imaging Algorithm

A. Imaging Geometry

The proposed method uses the data acquired from a MIMO radar mounted on a movable platform to synthesize a 3-D radar image. Radar data are collected while the platform travels in the along-track direction continuously.

Fig. 1 depicts a graphical illustration of the imaging geometry, wherein a 4×4 MIMO radar is traveling in the x-direction. In the figure, the illuminated scene is assumed to be near the origin, whereas the ground plane is considered normal to the z-axis. The four Tx and four Rx antennas, each illustrated in green and yellow, respectively, are positioned in the negative y-direction illuminating the origin.

The Tx channel is labeled as m, an integer varying from 1 to M, where M denotes the number of Tx channels. Similarly, the Rx channel is labeled as n varying from 1 to N, where N indicates the number of Rx channels.

In Fig. 1, the distances from the origin to the Tx and Rx antennas are denoted as $R_{tx,0}$ and $R_{rx,0}$, respectively. As the position of the antenna varies with the slow-time η, $R_{tx,0}$ and $R_{rx,0}$ also vary with η. $R_{tx,0}$ and $R_{rx,0}$ can be calculated as follows:

$$\begin{aligned} R_{tx,0}(\eta,m) &= \left|\left|\overrightarrow{P_{tx}(\eta,m)}\right|\right| \\ R_{rx,0}(\eta,n) &= \left|\left|\overrightarrow{P_{rx}(\eta,n)}\right|\right|. \end{aligned} \tag{1}$$

In (1), $\overrightarrow{P_{tx}(\eta,m)}$ and $\overrightarrow{P_{rx}(\eta,n)}$ denotes the position of the Tx and Rx antennas with channel numbers m and n, respectively, at slow-time η. $\left|\left|\overrightarrow{\cdot}\right|\right|$ denotes the 2-norm of $\left(\overrightarrow{\cdot}\right)$. Considering the position of a point scatterer $\overrightarrow{P_{target}}$ with Cartesian coordinates of (x,y,z), the distance from the antenna to the point scatterer can be calculated as

$$\begin{aligned} R_{tx}(m,\eta;x,y,z) &= \left|\left|\overrightarrow{P_{tx}(m,\eta)} - \overrightarrow{P_{target}}\right|\right| \\ R_{rx}(n,\eta;x,y,z) &= \left|\left|\overrightarrow{P_{rx}(n,\eta)} - \overrightarrow{P_{target}}\right|\right|, \end{aligned} \tag{2}$$

where R_{tx} and R_{rx} denotes the distances from the target to the Tx and Rx antennas, respectively.

B. BFD Signal Model and Demodulation

The number of radar channels can be increased by reducing the hardware complexity using the MIMO method. An increased number of channels was utilized to improve the cross-track resolution. The along-track resolution was limited by PRF [5]. To use the MIMO method without affecting PRF, radar signals should be transmitted and received simultaneously. Simultaneous reception of the radar signals can be achieved by designing individual Rx signal paths, using multiple or multichannel analog-to-digital converters (ADCs) and storing the radar data digitally. For simultaneous transmission, we propose using the BFD FMCW waveform.

In conventional FMCW radars, the backscattered signals and a duplicate of the transmitted signal pass through a frequency mixer to decrease the intermediate frequency bandwidth and ADC burden [33]. In the BFD FMCW method, multiple FMCW signals with equal chirp rates are transmitted simultaneously with each transmitted signal exhibiting slightly different center frequencies. Furthermore, the simultaneously backscattered signals pass through a frequency mixer similar to those of conventional FMCW radars. In this step, a duplicate of the transmit signal with the highest center frequency is input to the frequency mixer.

The reference signal s_{ref} used for the mixer input can be modeled as

$$s_{ref}(t) = \exp\left[j\left(2\pi f_0 t + \pi K_r t^2\right)\right], \tag{3}$$

where t represents the time variable varying from $-T_p/2$ to $T_p/2$, T_p denotes the pulse length, j indicates the imaginary unit, f_0 represents the center frequency of the reference signal, $K_r = \beta/T_p$ denotes the chirp rate, and β indicates the signal bandwidth. The transmit signal of channel m with a slightly different frequency offset can be modeled as follows:

$$s_{tx}(t,m) = \exp\left[j\left(2\pi\left(f_0 - f_{off}(m)\right)t + \pi K_r t^2\right)\right] \tag{4}$$

where $f_{off}(m)$ denotes the frequency offset of channel m, relative to the reference signal.

The transmit signal backscattered from a point scatterer and received at the Rx antenna was modeled as a time-delayed version of the transmitted signal [33]. The signal at the Rx antenna is modeled as a summation of time-delayed transmit signals since the multiple transmit signals simultaneously backscatter to the Rx antenna. The output of the frequency mixer was modeled as the multiplication of one input and a complex conjugate of the other input. Therefore, the mixer output s_{rx} of the Rx channel n can be modeled as

$$\begin{aligned} s_{rx}(t,n) &= A\sum_m s_{tx}(t - t_d(n,m),m)\cdot s^*_{ref}(t) \\ &\simeq A\sum_m \exp\left[-j2\pi(f_0 - f_{off}(m))t_d(n,m)\right] \\ &\quad \cdot\exp\left[-j2\pi(f_{off}(m) + K_r t_d(n,m))t\right], \end{aligned} \tag{5}$$

where A denotes the complex coefficient representing the scattering and path loss, and $t_d(n,m)$ indicates the channel-dependent time delay of the point scatterer.

According to the final expression in (5), s_{rx} is the summation of M single-tone signals. The frequency of the single-tone signal is $K_r t_d(n,m)$ which is lower than $f_{off}(m)$. The

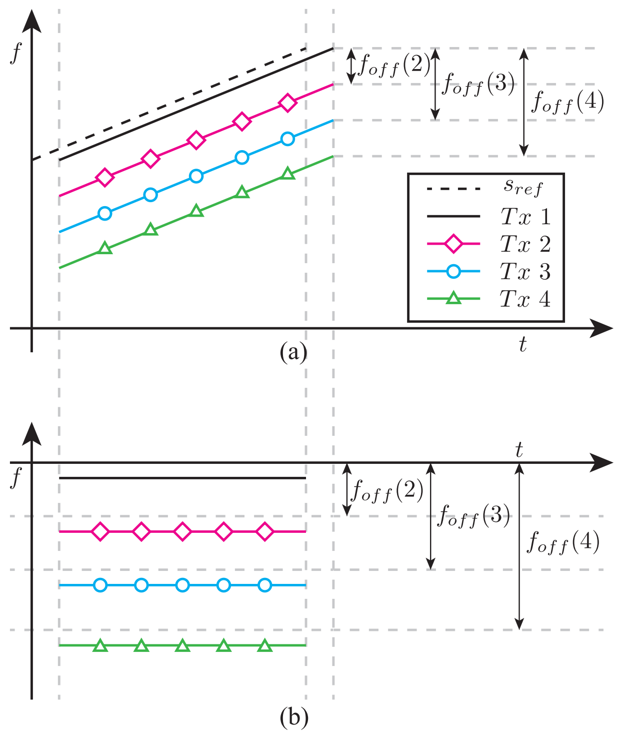

Fig. 2. Time-frequency diagram of a backscattered beat frequency division (BFD) frequency-modulated continuous wave (FMCW) signal with four Tx channels. The illustration shows the received signal (a) before and (b) after passing through the frequency mixer.

time-frequency diagram of the backscattered signals before and after passing through the frequency mixer is illustrated in Fig. 2 (a) and (b), respectively. In Fig. 2 (a), four time-delayed transmit signals are depicted as solid lines. The duplicate of the signal transmitted from Tx channel 1 is used as the reference signal s_{ref}, which is represented as a dashed line in the figure. After passing through the mixer, the four backscattered signals become single-tone signals, as depicted in Fig. 2 (b). The backscattered signal associated with the arbitrary channel m is $K_r t_d$ apart from $f_{off}(m)$. Herein, that $f_{off}(1)$ is zero because the duplicate of the transmit signal of Tx channel 1 is used as the reference signal.

Considering that the backscattered signal of the Tx channel m is close to $f_{off}(m)$ in the frequency domain, demodulation method can be established. To separate the signal of Tx channel m' from the receiver output, s_{rx} is multiplied by a sinusoidal.

$$\begin{aligned} &s_1(t,n,m') \\ &\quad= s_{rx}(t,n)\cdot\exp\left[j2\pi f_{off}(m')t\right] \\ &\quad= A\cdot\exp\left[-j2\pi\left(f_0 - f_{off}(m') + K_r t\right)t_d(n,m')\right] \\ &\qquad+ A\sum_{m\neq m'}\exp\left[-j2\pi\left(f_0 - f_{off}(m') + K_r t\right)t_d(n,m)\right] \\ &\qquad\cdot\exp\left[j2\pi\left(f_{off}(m) - f_{off}(m')\right)t\right] \end{aligned} \tag{6}$$

Subsequently, the Fourier transform is applied to s_1 in (6), resulting in

$$\begin{aligned} &s_2(f_t,n,m') \\ &\quad= AT_p\exp\left[-j2\pi(f_0 - f_{off}(m'))t_d(n,m')\right] \\ &\qquad\cdot\,\mathrm{sinc}\left[T_p\left(f_t + K_r t_d(n,m')\right)\right] \\ &\qquad+ AT_p\sum_{m\neq m'}\exp\left[-j2\pi\left(f_0 - f_{off}(m')\right)t_d(n,m')\right] \\ &\qquad\quad\cdot\,\mathrm{sinc}\left[T_p\left(f_t + K_r t_d(n,m) + f_{off}(m) - f_{off}(m')\right)t\right], \end{aligned} \tag{7}$$

where f_t denotes the frequency variable and $\mathrm{sinc}(\cdot) = \sin(2\pi\cdot)/(2\pi\cdot)$ indicates the sinc function. In (7), the response from m' lies between $f_t = 0$ and a negative maximum frequency. The response from the other channels can be filtered in the frequency domain by multiplying s_2 with the window function W, as follows:

$$W(f_t) = \begin{cases} 1, & -f_{t,max} < f_t \leq 0 \\ 0, & \text{otherwise} \end{cases}, \tag{8}$$

where $f_{t,max}$ denotes the maximum frequency that eliminates the response from other Tx channels and includes the frequency corresponding to the maximum time delay within the radar swath [2]. The frequency that satisfies such condition is $f_{t,max} < \Delta f_{off}$, where Δf_{off} denotes the minimum difference of $f_{off}(m)$ between different channels.

The output of the multiplication can be obtained as

$$\begin{aligned} &s_3(f_t,n,m') \\ &\quad= s_2(f_t,n,m')\cdot W(f_t) \\ &\quad= AT_p\exp\left[-j2\pi\left(f_0 - f_{off}(m')\right)t_d(n,m')\right] \\ &\qquad\cdot\,\mathrm{sinc}\left[T_p\left(f_t + K_r t_d(n,m')\right)\right]. \end{aligned} \tag{9}$$

In (9), it was assumed that $-K_r t_d > -f_{t,max}$. Since the time delay is proportional to range, the maximum achievable range is written as $R_{max} = c\Delta f_{off}/2K_r$, where R_{max} denotes the maximum range.

Demodulation is finalized by iterating the process for all channels and storing them. Equation (9) is a sinc function translated by $-K_r t_d$ in terms of frequency, which is proportional to the time delay of a point scatterer. By changing the variables from f_t to $\tau = -f_t/K_r$, the demodulated data are transformed into a form of the conventional pulse-compressed radar signal, represented as

$$\begin{aligned} &s_4(\tau,n,m) \\ &\quad= A'\exp\left[-j2\pi\left(f_0 - f_{off}(m)\right)t_d(n,m)\right] \\ &\qquad\cdot\,\mathrm{sinc}\left[\beta(\tau - t_d(n,m))\right], \end{aligned} \tag{10}$$

where τ denotes the fast-time variable, and A' indicates the trivial constants, including the target reflectivity, combined. For further algorithm derivations, (10) is Fourier transformed into the fast-time frequency domain, resulting in

$$\begin{aligned} &s_5(f_\tau,n,m) \\ &\quad= A'\exp\left[-j2\pi\left(f_0 - f_{off}(m) + f_\tau\right)t_d(n,m)\right] \end{aligned} \tag{11}$$

where f_τ denotes the fast-time frequency variable varying from $-\beta/2$ to $\beta/2$.

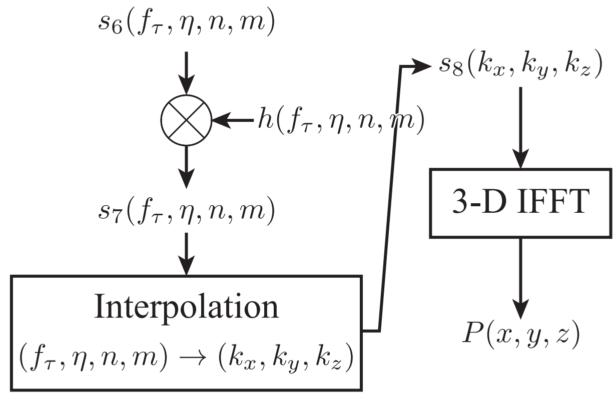

Fig. 3. Schematic of the three-dimensional (3-D) image formation algorithm.

C. 3-D Radar Imaging Algorithm Formulation

In (11), t_d denotes the travel time of the signal transmitted from Tx m, backscattered from a point scatterer, and received by Rx n. The travel time t_d is dependent on the slow-time η because the radar travels in the along-track direction. Assuming that the movement of radar from the signal transmission to reception is negligible, a stop-and-go approximation can be applied to t_d. Travel time t_d of a signal backscattered from a point scatterer at $\overrightarrow{P_{target}}$ can be obtained as

$$\begin{aligned} t_d(\eta, n, m; x, y, z) \\ = \frac{1}{c}\left[R_{tx}(m, \eta; x, y, z) + R_{rx}(n, \eta; x, y, z)\right], \end{aligned} \tag{12}$$

where R_{tx} and R_{rx} are defined in (2), and c denotes the speed of light.

R_{tx} can be expressed in terms of a range with respect to scene center, $R_{tx,0}$, by using trigonometric relationships, as follows:

$$\begin{aligned} R_{tx}(m, \eta; x, y, z) = \Big[& R^2_{tx,0}(m, \eta) + (x^2 + y^2 + z^2) \\ & - 2R_{tx,0}(m, \eta)\sin[\theta_{tx,0}(m, \eta)]\cos[\phi_{tx,0}(m, \eta)]x \\ & - 2R_{tx,0}(m, \eta)\sin[\theta_{tx,0}(m, \eta)]\sin[\phi_{tx,0}(m, \eta)]y \\ & - 2R_{tx,0}(m, \eta)\cos[\theta_{tx,0}(m, \eta)]z \Big]^{1/2}, \end{aligned} \tag{13}$$

where $\theta_{tx,0}$ and $\phi_{tx,0}$ denote the polar and azimuth angles of $\overrightarrow{P_{tx,0}}$, respectively, dependent on slow-time. A graphical illustration of θ and ϕ is represented in Fig. 1 in red regions.

Assuming that the Tx antenna is far from the scene center in comparison with the position of the point scatterer, the Taylor expansion can be applied to (13), resulting in

$$\begin{aligned} R_{tx}(m, \eta; x, y, z) \simeq & R_{tx,0}(m, \eta) \\ & - \sin[\theta_{tx,0}(m, \eta)]\cos[\phi_{tx,0}(m, \eta)]x \\ & - \sin[\theta_{tx,0}(m, \eta)]\sin[\phi_{tx,0}(m, \eta)]y \\ & - \cos[\theta_{tx,0}(m, \eta)]z. \end{aligned} \tag{14}$$

Using a similar method, R_{rx} can be approximated as

$$\begin{aligned} R_{rx}(n, \eta; x, y, z) \simeq & R_{rx,0}(n, \eta) \\ & - \sin[\theta_{rx,0}(n, \eta)]\cos[\phi_{rx,0}(n, \eta)]x \\ & - \sin[\theta_{rx,0}(n, \eta)]\sin[\phi_{rx,0}(n, \eta)]y \\ & - \cos[\theta_{rx,0}(n, \eta)]z, \end{aligned} \tag{15}$$

where $\theta_{rx,0}$ and $\phi_{rx,0}$ denote the polar and azimuth angles of $\overrightarrow{P_{rx,0}}$, respectively.

By combining (11), (12), (14), and (15), the demodulated signal backscattered from a single point scatterer can be modeled. The backscattered response of a complex scene is modeled as the summation of signals from multiple point scatterers. Assuming L scatterers within the illuminated scene, the demodulated signal can be modeled as follows:

$$\begin{aligned} & s_6(f_\tau, \eta, n, m) \\ & = \sum_l A'_l \exp\Big[-j\frac{2\pi}{c}\left(f_0 - f_{off}(m) + f_\tau\right) \\ & \quad \cdot \left(R_{tx}(m, \eta; x_l, y_l, z_l) + R_{rx}(n, \eta; x_l, y_l, z_l)\right)\Big] \\ & = \exp\left[-jk_r\left[R_{tx,0}(m, \eta) + R_{rx,0}(n, \eta)\right]\right] \\ & \quad \cdot \left[\sum_l A'_l \exp\left[-j(k_x x_l + k_y y_l + k_z z_l)\right]\right], \end{aligned} \tag{16}$$

where l denotes the index of the individual scatterers. Variables k_r, k_x, k_y, and k_z are defined as

$$\begin{aligned} k_r &= \frac{2\pi}{c}\left(f_0 + f_{off}(m) + f_\tau\right) \\ k_x &= -k_r\big[\sin[\theta_{tx,0}(m, \eta)]\cos[\phi_{tx,0}(m, \eta)] \\ & \quad + \sin[\theta_{rx,0}(n, \eta)]\cos[\phi_{rx,0}(n, \eta)]\big] \\ k_y &= -k_r\big[\sin[\theta_{tx,0}(m, \eta)]\sin[\phi_{tx,0}(m, \eta)] \\ & \quad + \sin[\theta_{rx,0}(n, \eta)]\sin[\phi_{rx,0}(n, \eta)]\big] \\ k_z &= -k_r\big[\cos[\theta_{tx,0}(m, \eta)] + \cos[\theta_{rx,0}(n, \eta)]\big]. \end{aligned} \tag{17}$$

To separate the individual scatterers in the 3-D space, a filter h referenced to the scene center is defined using $R_{tx,0}$ and $R_{rx,0}$, as follows:

$$\begin{aligned} & h(f_\tau, \eta, n, m) \\ & \quad = \exp\left[jk_r\left(R_{tx,0}(m, \eta) + R_{rx,0}(n, \eta)\right)\right]. \end{aligned} \tag{18}$$

The filter h is multiplied with the demodulated data s_6, resulting in

$$\begin{aligned} & s_7(f_\tau, \eta, n, m) \\ & \quad = s_6(f_\tau, \eta, n, m) \cdot h(f_\tau, \eta, n, m) \\ & \quad = \sum_l A'_l \exp\left[-j(k_x x_l + k_y y_l + k_z z_l)\right]. \end{aligned} \tag{19}$$

In (19), s_7 can be Fourier transformed in k_x, k_y, and k_z to separate the individual scatterers in Cartesian grid (x, y, z). In this step, the data can be initially interpolated to a uniform (k_x, k_y, k_z) to utilize the efficient computation of FFT. As a result, the computational load of the data processing may be controlled by the required accuracy of the interpolation.

The data processing of the proposed algorithm is depicted in Fig. 3. According to the figure, the data is interpolated into a uniform k_x, k_y, and k_z grid for efficient processing. Conceptually, the data before the interpolation is a four-dimensional data with multiple data cubes. After the interpolation, the data is interpolated into a data cube with k_x, k_y, and k_z being the three dimensions.

According to (17) the slow-time varying $\overrightarrow{P_{tx}}$ and $\overrightarrow{P_{rx}}$ are required to properly interpolate the data and generate the

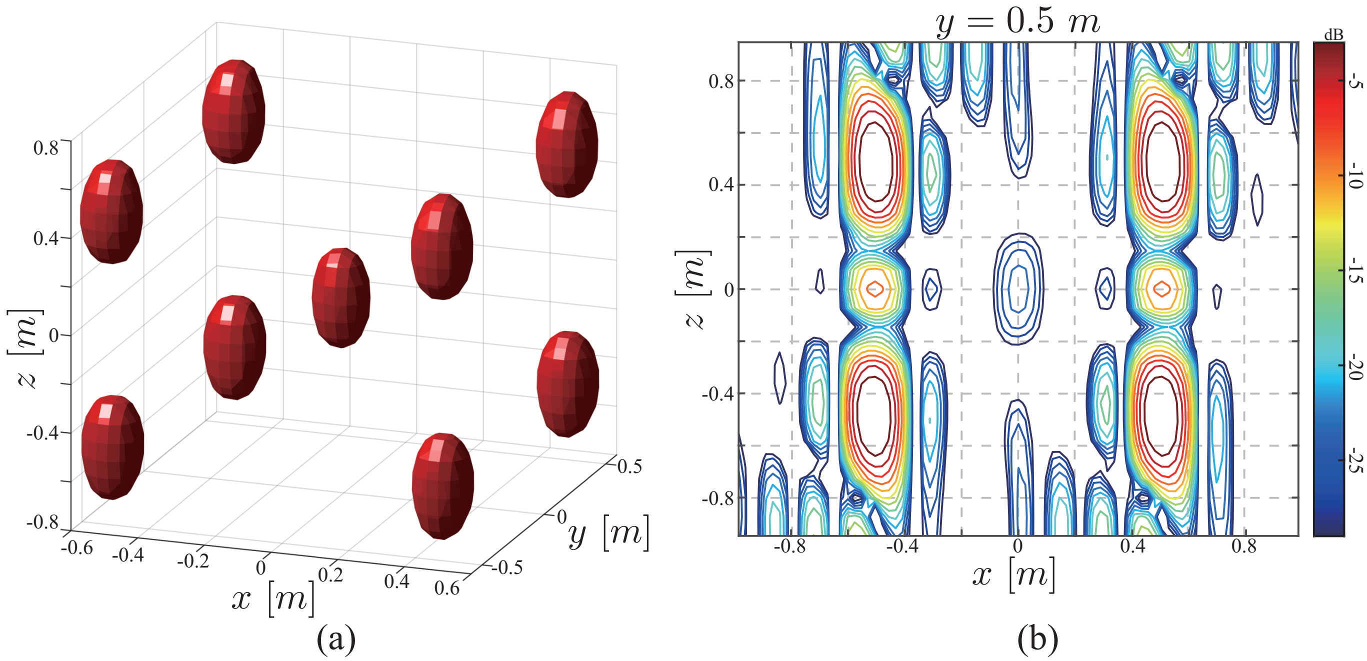

Fig. 4. Three-dimensional (3-D) radar imaging result of the proposed method applied to simulated data assuming nine point scatterers. (a) -10 dB isosurfaces illustrated on a 3-D projection grid indicating nine scatterers at the corners and center of a cuboid. (b) Isocontours of the imaging result at $y = 0.5$ m with four peaks at the corners.

radar image. The positions of the channels relative to the scene center can either be measured using positioning systems or modeled using platform movement. Assuming a linear platform motion with a velocity vector $\overrightarrow{v}$, the position of the antenna can be modeled as $\overrightarrow{P_m} + \eta\overrightarrow{v}$ or $\overrightarrow{P_n} + \eta\overrightarrow{v}$, where $\overrightarrow{P_m}$ and $\overrightarrow{P_n}$ denote a position that the transmit or receive antennas, respectively, passes.

The proposed method uses the Fourier transform to synthesize a 3-D radar image. Therefore, a uniform data measurement in the range, along-track, and cross-track directions is required for superior imaging performance. These criteria can be satisfied by transmitting a linear frequency-modulated waveform in the range direction, and maintaining a constant velocity in the along-track direction. In the cross-track direction, the Tx and Rx antennas should be positioned appropriately considering the platform movement and illumination direction to achieve uniform data measurement in k_x, k_y, and k_z.

According to (17), the interpolation kernel does not depend on the array configuration. As a result, the proposed algorithm may be applied to BFD FMCW radars with arbitrary array configurations, including planar arrays. The usage of planar arrays may be exploited to enable dense cross-track data measurements with larger antennas, which can be used to improve the quality such as the signal-to-noise ratio (SNR) of the final image.

Due to the approximation in (14) and (15), the imaging size of the proposed method is limited. Following the discussion by Rigling et al., the imaging size is limited in the range and cross-track directions by the length of the antenna movement and cross-track span of the antenna array [30].

TABLE I
RADAR PARAMETERS

Parameters	Units	Value			
		Tx 1	Tx 2	Tx 3	Tx 4
waveform	-	BFD FMCW			
f_0	GHz	94			
β	GHz	1			
f_{off}	MHz	0	2	0	2
T_p	ms	1			
PRF	Hz	500			

III. NUMERICAL SIMULATION

A. Simulation Parameters

Simulated radar data were generated for numerical experiments to demonstrate the effectiveness of the proposed method. The simulation parameters were referenced from an operating W-band MIMO radar, as previously reported by Jeon et al. [2]. The referenced hardware is a 4×4 MIMO radar that utilizes a TDM–FDM hybrid signal transmission scheme. According to Jeon et al., Tx 1 and Tx 2 are transmitted simultaneously, followed by the simultaneous transmission of signal from Tx 3 and Tx 4. The simultaneously transmitted signals use the BFD FMCW waveform.

The hardware reported by Jeon et al. was a high-resolution radar with a bandwidth larger than 1 GHz [2]. The parameters for radar data generation were selected within the hardware capabilities of actual experiments. Table I lists the radar parameters employed in the simulation; the center frequency difference between the simultaneously transmitted signals was 2 MHz.

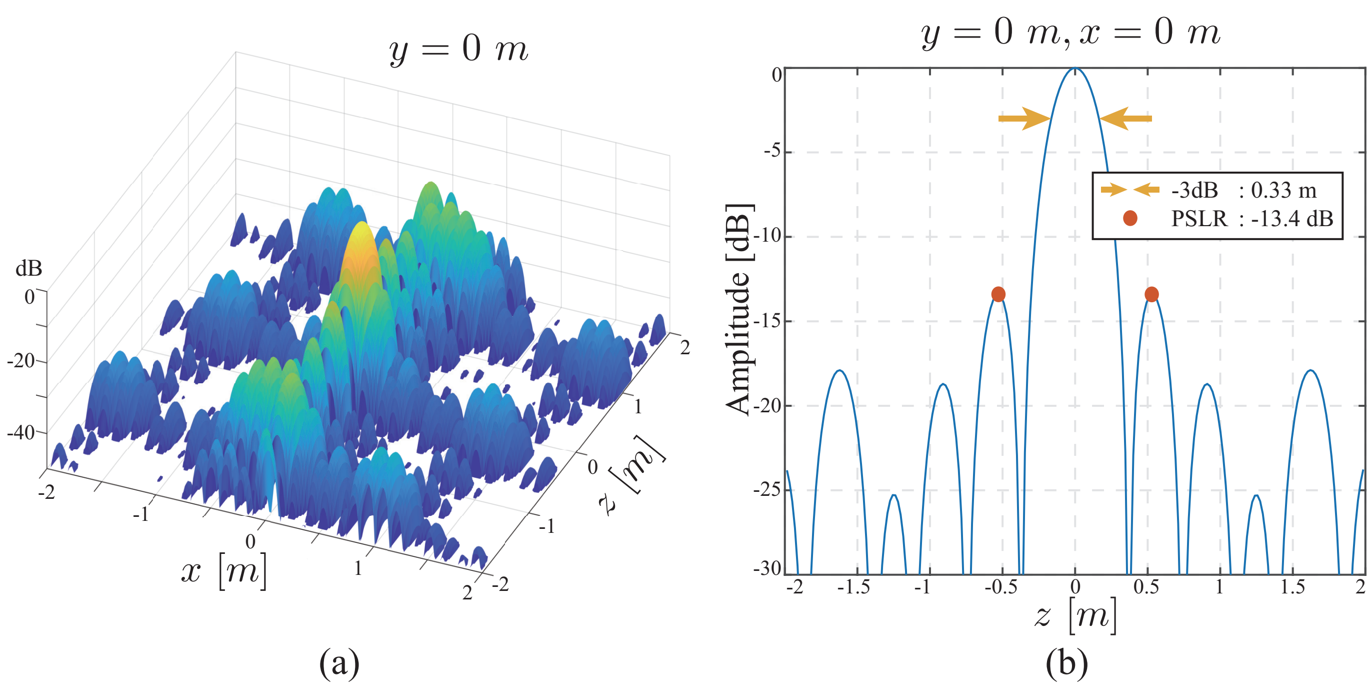

Fig. 5. Three-dimensional (3-D) radar imaging result of the proposed method applied to simulated data assuming a single point scatterer. (a) Imaging result at $y = 0$ m with a single peak at the center of the illustration. (b) A profile of the imaging result in the z-direction at $y = 0$ m, $x = 0$ m.

The simulation geometry assumed a radar operation similar to that depicted in Fig. 1, where the negative x-direction indicates the direction of radar movement. Assuming a side-looking broadside measurement, the radar LOS was considered to be parallel to the y-axis. Accordingly, the z-direction was the cross-track direction perpendicular to the ground plane. The radar was placed 45 m from the scene center in the negative y-direction, and the platform was moved at 0.1 m/s for 5 s considering real data acquisition.

As explained in Section II, uniform data measurement in the cross-track direction is required for superior imaging performance. The experimental configuration reported by Jeon et al. resulted in the overlapping tracks of the Tx and Rx antennas [2]. Therefore, in the numerical simulation, the radar was assumed to be rotated by 15 ° from the ground plane to effectively utilize data from 16 MIMO radar channels. The resultant (x, z) coordinates of the Tx and Rx antennas are depicted in Fig. 8 (d).

Considering the experimental conditions, the span of the data in k_x is calculated as follows:

$$k_{z,max} - k_{z,min} \simeq \frac{2\pi}{c} f_0 \left[\frac{z_{tx,1} - z_{tx,4}}{R} + \frac{z_{rx,1} - z_{rx,4}}{R} \right] = 16 \text{ rad/m}, \tag{20}$$

where $k_{z,max}$ and $k_{z,min}$ denote the maximum and minimum value of the data in k_z, respectively, $z_{tx,1}$, $z_{tx,4}$, $z_{rx,1}$, and $z_{rx,4}$ denote the z-coordinate of Tx 1, Tx 4, Rx 1, and Rx 4, respectively, and R denotes the approximate range from the radar to the scene center. The expected resolution of the numerical experiment corresponding to the span of the data is 0.33 m. The four channels used to calculate the span of the data represents the positions of Tx and Rx antennas with minimum and maximum coordinates in the cross-track direction. The equation implies that the cross-track resolution is inversely proportional to the ratio between the array size in the cross-track direction and the wavelength of the transmitted signal. The property of the cross-track resolution is especially beneficial for millimeter waves with short wavelengths since the size and weight of the antenna array are usually limited by the platform size and payload.

B. Simulation Results

To verify the 3-D imaging capabilities of the proposed method, we considered nine point scatterers with identical reflectivity. The coordinates of eight scatterers were $(\pm 0.5 \text{ m}, \pm 0.5 \text{ m}, \pm\ 0.5 \text{ m})$ which corresponded to the corners of a cuboid centered at the origin. The remaining scatterer was assumed to be positioned at the origin.

Fig. 4 depicts the 3-D imaging results of the numerical simulation. In Fig. 4 (a), -10 dB isosurfaces of the imaging result are depicted on a 3-D projection grid to approximately show the localization of the individual scatterers in the volumetric space. The isosurfaces appear distributed in the volumetric space as nine ellipsoids. The positions of the eight ellipsoids correspond to the corners of a cuboid, which concur with the experimental conditions. Therefore, the results verify that the 3-D microwave imaging is possible using the proposed method.

To analyze the imaging results further, an $x - z$ slice of the imaging result at $y = -0.5$ m was used to depict an isocontour map. The slice corresponds to a plane 0.5 m closer to the radar from the scene center in the range direction. According to the experimental conditions, four point scatterers existed on this plane. Fig. 4 (b) depicts the isocontour map,

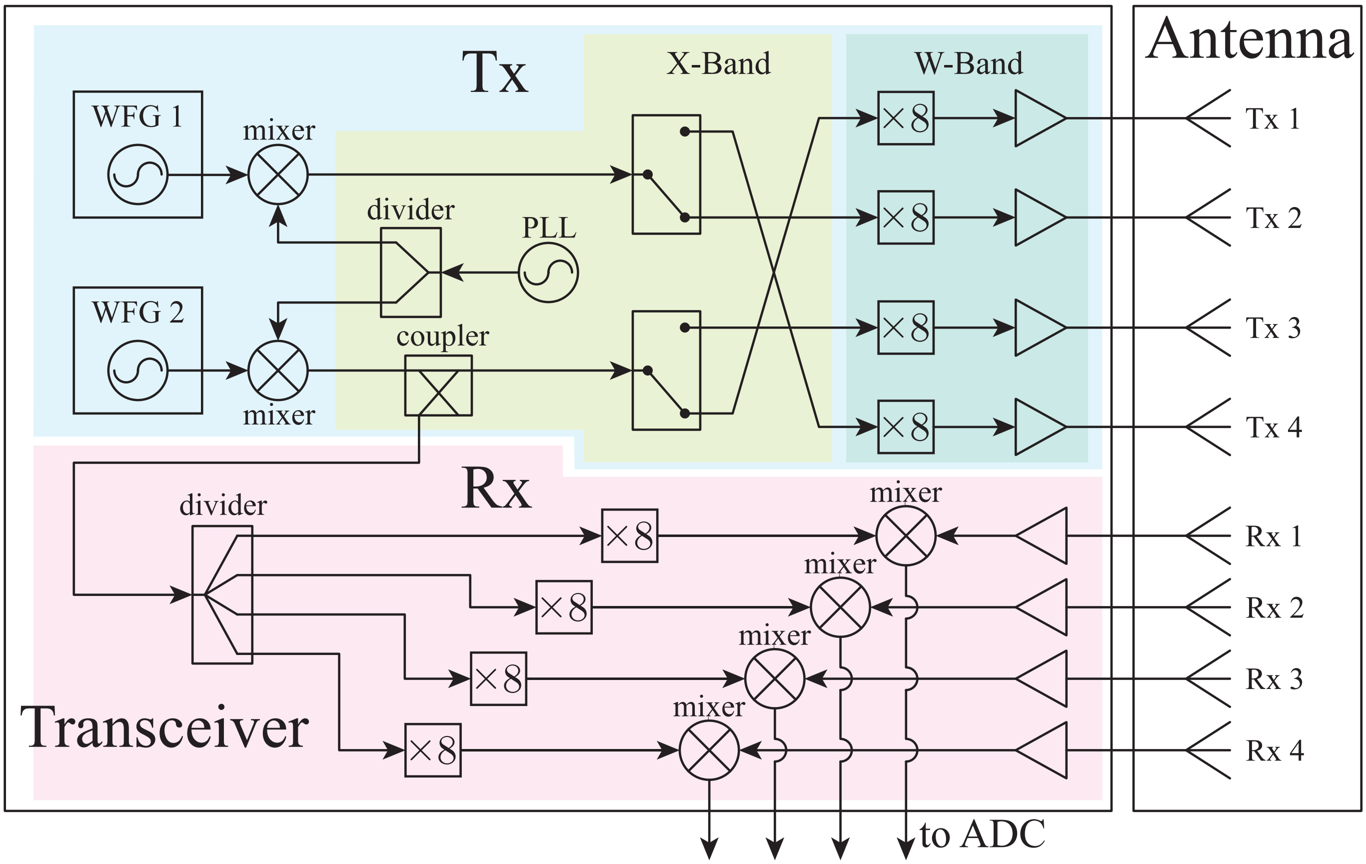

Fig. 6. Functional diagram of the 4 × 4 multiple-input multiple-output (MIMO) frequency-modulated continuous wave (FMCW) radar transceiver. The Tx and Rx functions are indicated in blue and red, respectively. The transmit signals with different center frequencies are generated from individual waveform generators (WFGs).

where four peaks can be observed at the (x, z) coordinates of $(\pm 0.5\text{ m}, \pm 0.5\text{ m})$. According to the experimental conditions, two pairs of point scatterers with the same x-coordinates exist on this plane. Individual scatterers should be resolved in the z-direction, which corresponds to the cross-track direction. In Fig. 4 (b), the four scatterers can be individually localized by the positions of the peaks, validating the resolution capability of the proposed method in the cross-track direction.

To analyze the cross-track imaging performance of the proposed method, a single point scatterer located at the origin was used to generate a simulated radar data. In Fig. 5 (a), imaging result of the single target simulation at $y = 0$ m was depicted on a 3-D surface. The position of the single point scatterer can be identified by the single peak observed at the center of the image. Fig. 4 (d) depicts a cross-track profile of the isocontour map using the response at $x = 0$ m. The measured -3 dB resolution of the image in the cross-track direction was 0.33 m which concurs with the expected value. The peak sidelobe level was measured to be -13.4 dB.

IV. 3-D Radar Imaging Experiment

A. Radar Data Acquisition

To validate the proposed method further, the 3-D radar imaging algorithm was applied to the data acquired from a functional W-band MIMO radar. Table I lists the hardware parameters of the radar. In Table I, PRF denotes the frequency of the transmission with regards to a single channel. Considering the frequency offset due to BFD waveform, the maximum range of the experiment setup was 299.8 m.

Fig. 6 illustrates a functional diagram of the radar transceiver wherein the transmission function of the transceiver is shaded blue. The radar transceiver uses a TDM–FDM hybrid transmission scheme for the signal transmission. According to the switch in Fig. 6, the signals from Tx 1 and Tx 2 are transmitted simultaneously. In the subsequent transmission, signals from Tx 3 and Tx 4 are transmitted simultaneously by altering the two switch outputs. The switch output is altered for each pulse transmission, facilitating the TDM–FDM hybrid transmission.

The simultaneously transmitted signals are generated from individual waveform generators (WFGs) with slightly different center frequencies, separating the of transmitting channels in the frequency domain. In Fig. 6, the signal from WFG 1 has a lower center frequency than WFG 2. Consequently, the center frequencies of the signals transmitted from Tx 1 and Tx 3 were 2 MHz lower than those transmitted from Tx 2 and Tx 4.

As explained in Section II, the received signal passes through a frequency mixer, as depicted in Fig. 6. The reference signal to the frequency mixer is a duplicate of the signal generated from WFG 2, which are the signals transmitted from Tx 1 and Tx 3. The output of the frequency mixer was

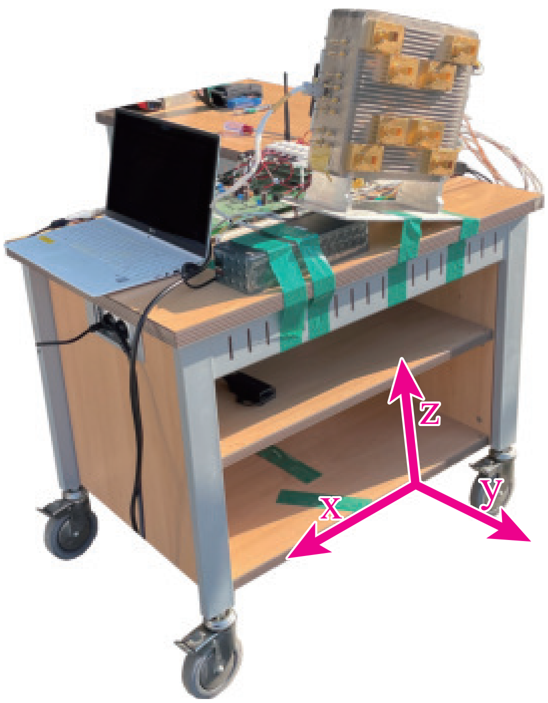

(a)

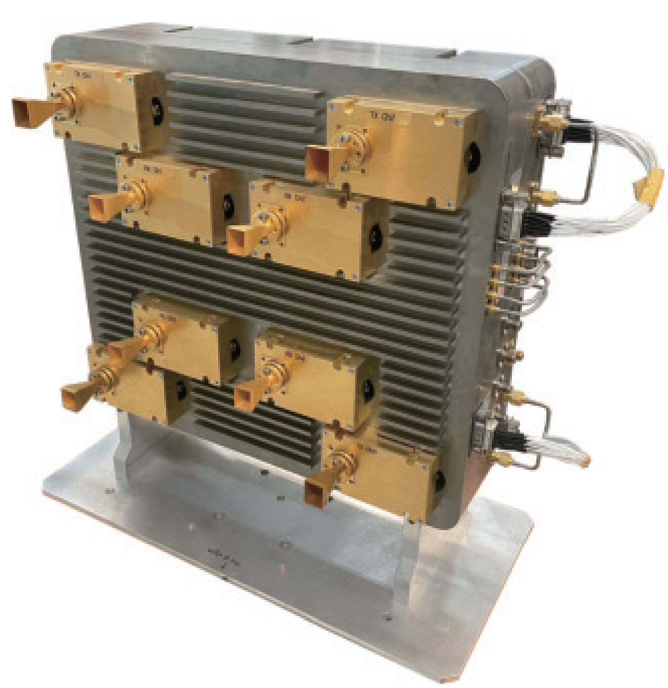

(b)

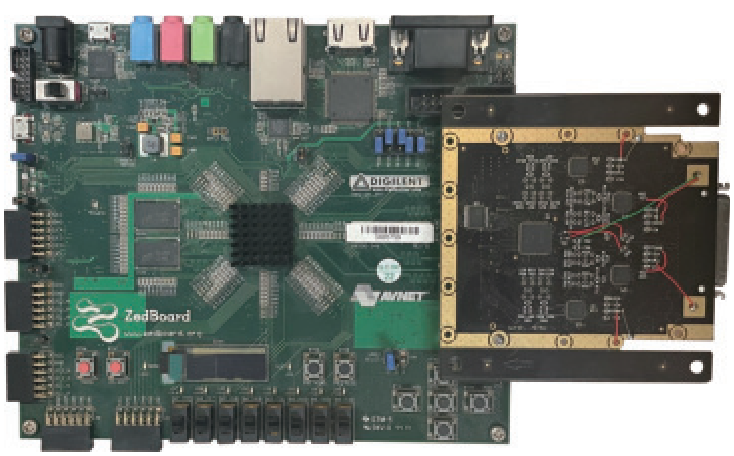

(c)

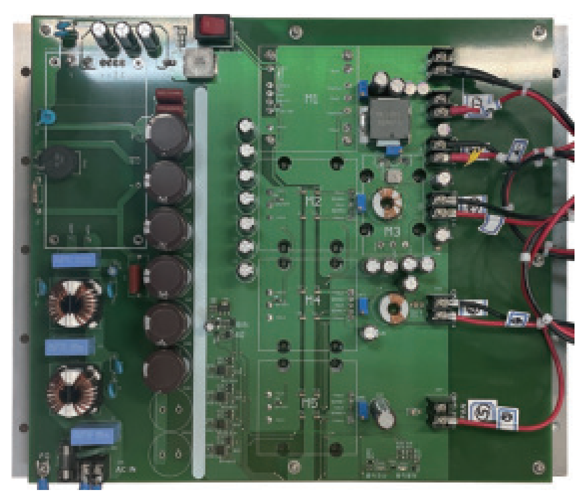

(d)

Fig. 7. Images of the radar hardware and platform. (a) Radar hardware mounted on the movable platform. (b) Radar transceiver equipped with gold-plated W-band antenna. (c) Signal processor that performs the synchronous analog-to-digital conversion. (d) Power board that provides the necessary voltage to the hardware components.

connected to the ADC in the signal processor via an SMA cable. Subsequently, the simultaneously transmitted signals were digitally separated in the frequency domain.

To employ the proposed method, radar hardware was mounted on a rectangular table with wheels. Fig. 7 (a) depicts a perspective view of the hardware setup, wherein the radar transceiver, signal processor, power board, and control PC are mounted on a movable table.

Fig. 7 (b) presents a detailed image of the radar transceiver. The circuits used to realize the function shown in Fig. 6 are enclosed in a steel casing with heat-radiating patterns. The realization and performance of the circuits are described in a previous study [1], [2]. Furthermore, gold-plated W-band antennas were equipped with a WR-10 waveguide at the front of the transceiver.

Fig. 7 (c) depicts a top-down image of the signal processor. The signal processor performs synchronous analog-to-digital conversion of the transceiver output and transmits the digital data to the control PC. The analog-to-digital conversion of the multichannel output was realized using a four-channel ADC circuit. To synchronously convert the transceiver output, a reference clock and trigger signal from the transceiver are input to the signal processor. To realize digital data transmission to the control PC, an Ethernet connection and an on-board operating system that can access digitally stored data were utilized.

In the radar imaging experiment performed by Jeon et al.

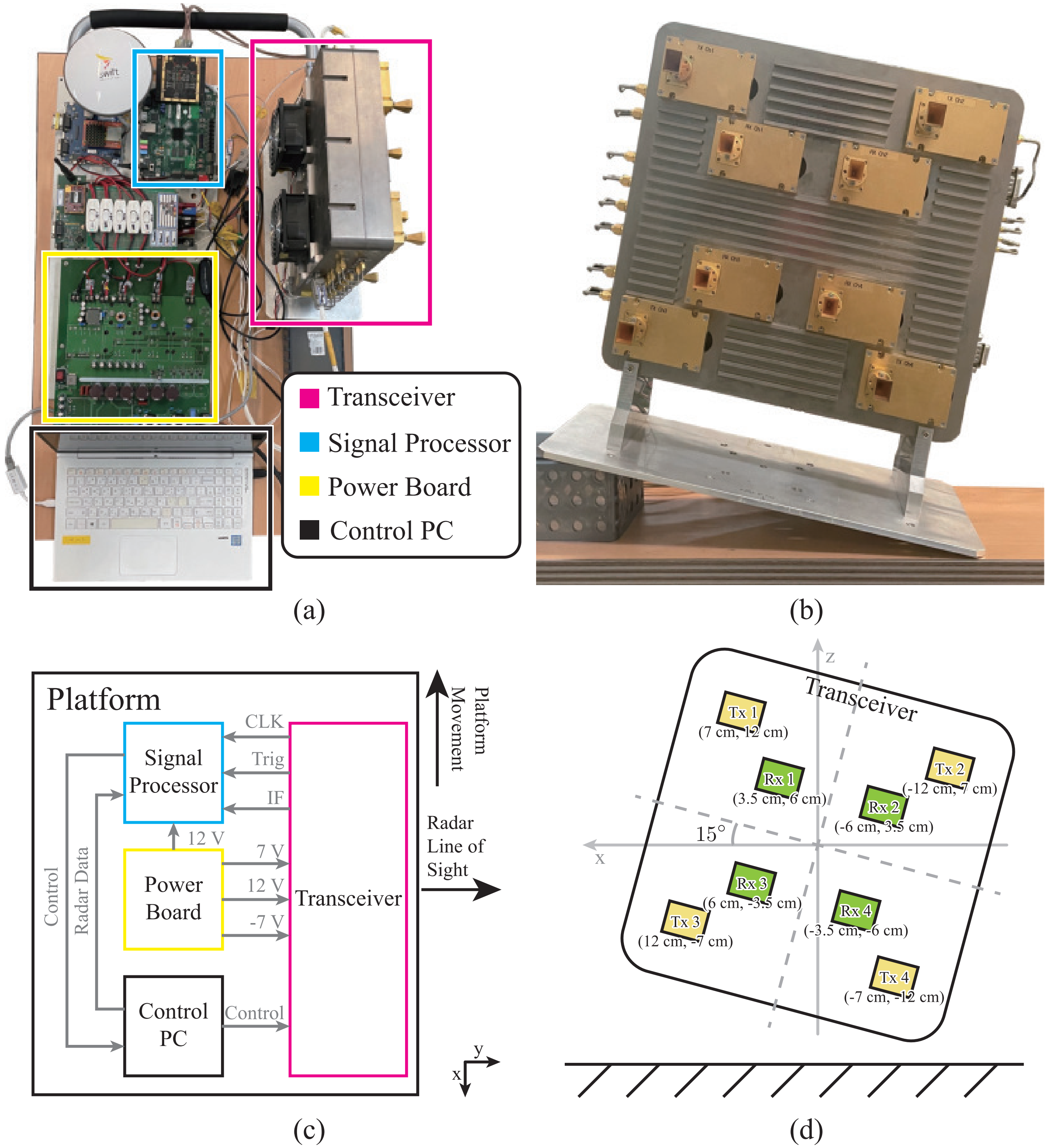

Fig. 8. Images and diagrams of the experimental setup. (a) Top-down image of the radar hardware mounted on the platform. (b) Radar transceiver in the radar line of sight (LOS) direction. (c) Hardware setup illustrated on the $x-y$ plane indicating the radar LOS and the along-track directions. (d) Radar transceiver illustrated on a plane parallel to the $x-z$ plane indicating the (x, z) coordinates of the antenna.

[2], four 12 V batteries were used to provide a 48 V DC power to the radar hardware. Therefore, the total operation time was limited by the battery capacity. A power board that converts 220 V AC to DC power was designed to ease the data acquisition. Fig. 7 (d) depicts a photograph of the power board, which can utilize common electrical outlets to provide the DC required to operate the radar hardware.

As stated earlier, radar was mounted on a rectangular table with wheels. The edge of the table was used to realize linear radar motion. To minimize the radar vibration during motion,

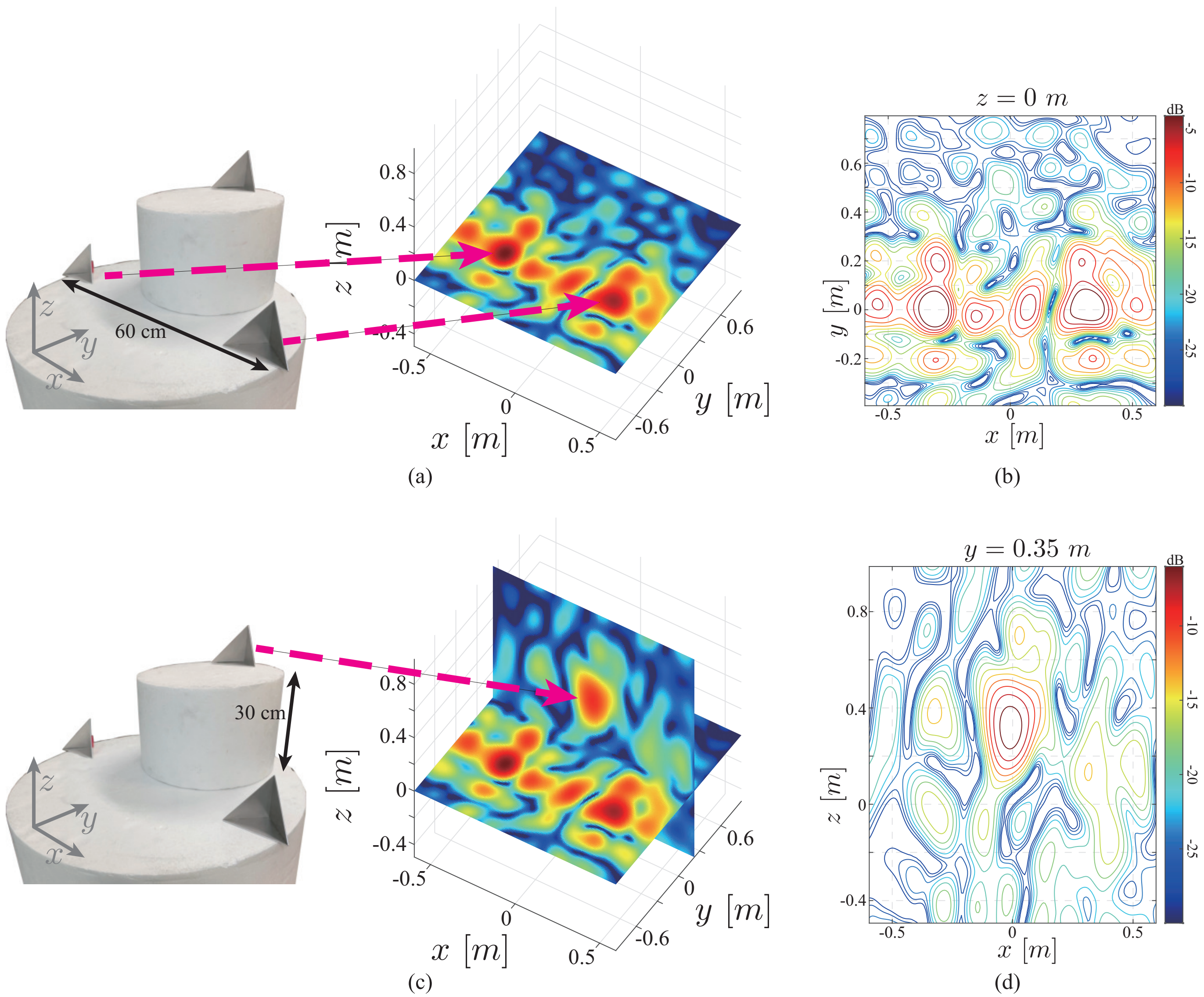

Fig. 9. Three-dimensional (3-D) radar imaging results of the proposed method applied to the data acquired from corner reflectors. (a) An $x-y$ slice of the imaging result at $z=0$ m in the 3-D projection view. (b) Isocontours of the $x-y$ slice at $z=0$ m representing the response from two corner reflectors. (c) An $x-z$ slice of the imaging result at $y=0.35$ m in 3-D projection view. (d) Isocontours of the $x-z$ slice at $y=0.35$ m indicating the response from a single corner reflector.

the experiment was performed on a smooth ground in the Yonsei University campus, Republic of Korea. Radar data were acquired for 5 s while moving at a speed of 0.1 m/s. The target was placed 45 m from the radar. According to the SAR principle, movement of 0.5 m corresponds to an azimuth resolution of 14 cm in the 45 m range. Additionally, the simulation indicated that the resolution in the height direction was 33 cm.

In the previous work by Jeon et al., the data acquisition was performed using a ground vehicle on an irregular surface [2]. As a result, phase error due to motion error required compensation to properly synthesize the radar image. On the other hand, the phase compensation was not adopted in this paper due to sufficiently smooth track and the slow velocity.

The time interval between two consecutive BFD FMCW signals is 1 ms. The movement of the platform during the interval is 0.1 mm. As a result, the movement within one pulse repetition interval was considered negligible when applying the proposed algorithm to the measurement data.

Given the PRF, the maximum velocity to synthesize a SAR image with azimuth resolution of 14 cm is 70 m/s. Nevertheless, to demonstrate the cross-track imaging capability of the proposed method, a sufficiently small velocity was used for the experiment.

Fig. 8 (a) depicts a top-down image of the radar hardware mounted on the platform. Fig. 8 (c) illustrates a diagram of the hardware setup, including the hardware connections. The transceiver was mounted on the platform with the radar LOS perpendicular to the platform movement to obtain broadside measurement of the radar data. To apply the 3-D imaging algorithm to the measured data, the platform movement and LOS directions were assumed to be parallel to the x- and y-

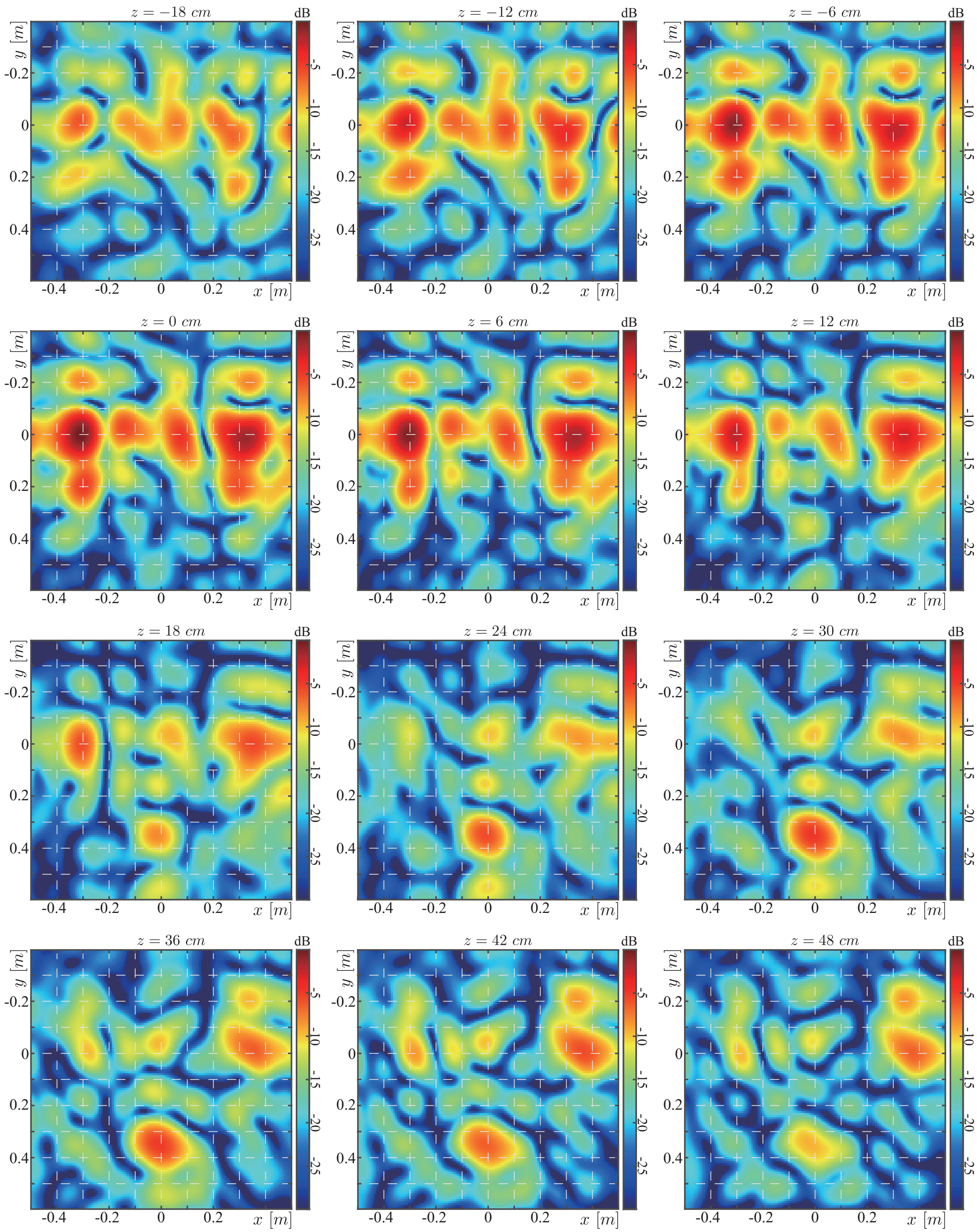

Fig. 10. Twelve $x - y$ slices of the three-dimensional (3-D) imaging result from $z = -18$ cm to $z = 48$ cm.

axes, respectively. The resultant geometry of the experimental setup is illustrated in Fig. 8 (c) with black arrows.

As explained in Section II, a uniform distribution of data in the cross-track direction is preferred for obtaining superior imaging results. Therefore, to prevent the overlapping of antenna positions, the radar hardware was rotated by $15\ ^\circ$ with respect to the radar LOS direction throughout the experiment. Fig. 8 (b) depicts the resultant image of the radar hardware obtained from the radar LOS direction. Fig. 8 (d) illustrates a diagram of the antenna geometry on a plane parallel to the $x - z$ plane; the (x, z) coordinates of the antenna locations are also presented, which can be used to identify $\overrightarrow{P_m}$ and $\overrightarrow{P_n}$.

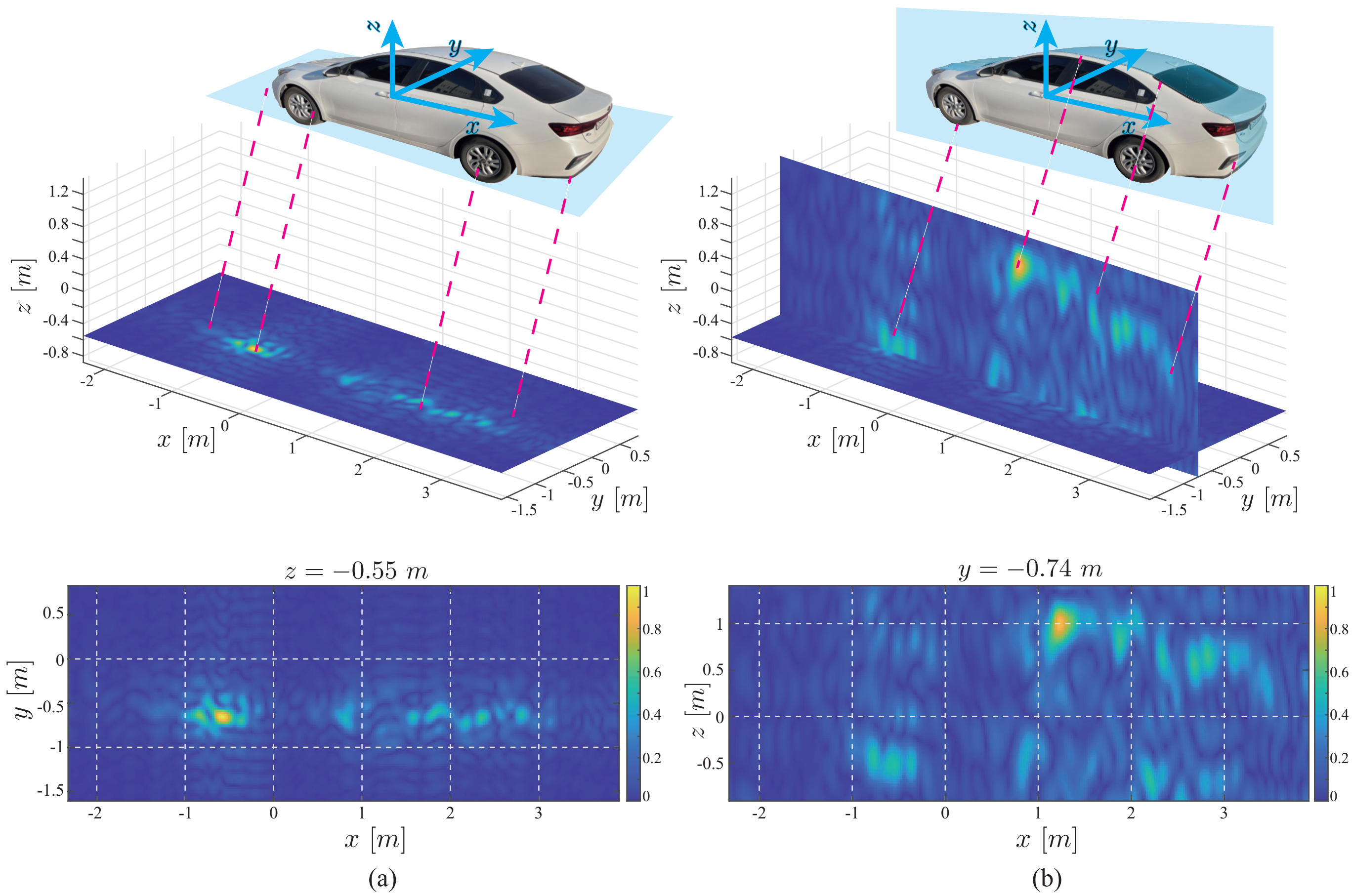

Fig. 11. Three-dimensional (3-D) radar imaging result of the proposed method applied to the data acquired from the target vehicle. (a) An $x-y$ slice of the imaging result at $z=-0.55$ m (bottom) and the slice illustrated on a 3-D projection grid (top). (b) An $x-z$ slice of the imaging result at $y=-0.74$ m (bottom) and the slice illustrated on a 3-D grid (top)

Thereafter, the position of the moving antennas are modeled using a velocity vector with zero y- and z- components.

Owing to certain error sources such as different signal paths, differences in RF module characteristics, and waveform generator phase offsets, the demodulated data obtained from 16 radar channels exhibit amplitude and phase differences. To calibrate the phase and amplitude of the channels, the radar data from a point target were acquired without radar movement. A trihedral corner reflector with radar cross section (RCS) of 50 m^2 was placed on the radar LOS at 25 m. The radar channels were calibrated using a calibration matrix that equalized the amplitude and phase of the point target.

B. Experiment Results

1) Point Target Experiments: Radar data were acquired using three triangular trihedral corner reflectors with an RCS of 50 m^2. The corner reflectors were distributed in the volumetric space by placing them on a cylindrical support composed of polystyrene foam. Fig. 9 depicts an image of the three corner reflectors. Considering the previous radar imaging experiments by Jeon et al. with longer target range, less number of channels, and lower target RCS, it was considered that the transmit power of the radar would provide sufficient SNR to generate 3-D images of the target [1], [2].

As indicated in the figure, two corner reflectors were placed on the same cylindrical support at the same height from the ground. They were separated in the along-track direction by a distance of 60 cm. Another cylindrical support with a smaller base diameter and a height of 30 cm was placed on top of the aforementioned support to place another corner reflector at a different height. Consequently, the third corner reflector was 30 cm further and higher in the range and cross-track directions, respectively, than the other corner reflectors. The set of corner reflectors was placed 45 m from the radar hardware. The experiment was performed by continuously moving the radar at a low speed.

Fig. 9 (a) depicts the $x-y$ slice of the imaging result at $z=0$ m on a 3-D projection grid. As the height of the radar hardware is identical to that of the large cylindrical support, the $z=0$ m plane corresponds to the plane that includes the two corner reflectors with the same height. The figure indicates two large responses separated in the x-direction, which correspond to the locations of the two corner reflectors separated in the along-track direction. The responses from the two corner reflectors are indicated by red arrows in the figure.

Fig. 9 (b) illustrates an isocontour map of the imaging results at $z=0$ m. The two peaks corresponding to the responses from the two corner reflectors are apparent at the

(x, y) coordinates of $(-30\ cm, 1\ cm)$ and $(30\ cm, 7\ cm)$. The distance of 60 cm between the two peaks matches with the experimental conditions.

Fig. 9 (c) depicts the $x-z$ slice of the imaging result at $y = 0.3$ m on the 3-D projection grid illustrated in Fig. 9 (a). The result in Fig. 9 (b) indicates that no distinct response exists at $y = 0.3$ m, which corresponds to the distance of 30 cm further from the locations of the two corner reflectors. According to Fig. 9 (c), a large response is present at a location 30 cm above the $z = 0$ m plane. This response is the reflection from the corner reflector placed on the smaller cylindrical support. The response from the corner reflector is indicated by the red arrow in the figure.

2) Ground Vehicle Experiments: To analyze the imaging results further, an isocontour map of the $x-z$ slice is depicted in Fig. 9 (d). Herein, a single peak can be observed at the (x, z) coordinates of $(-1$ cm, 32 cm$)$. The z-coordinate of the response corresponds to the height of the smaller cylindrical support, validating the cross-track imaging capability of the proposed method.

The -3 dB resolution in the z-direction measured from the peak in Fig. 9 (d) is 34 cm, which concurs with the simulation results presented in Section III. The measured peak sidelobe level was $-8.9\ dB$, which was $4.5\ dB$ larger than the value reported in the numerical simulation. This difference can be attributed to the reflection generated by the side of the cylindrical support.

To analyze the 3-D imaging result further, 12 $x-y$ slices of the imaging result from $z = -18$ cm to 48 cm was depicted in Fig. 10. The slices corresponded to the planes that were parallel to the ground plane. The backscattered information from different heights can be compared and analyzed based on the sequential arrangement of multiple images. The location of the first slice ($z = -18$ cm) corresponds to a plane 18 cm below the radar hardware. According to the image, no distinct response exists on this plane.

According to the second slice in Fig. 10 ($z = -12$ cm), two large responses appear as two peaks, separated by 60 cm in the x-direction. The magnitude of the response increased with the increase in the height of the slice. The magnitude of the peak attains a maximum value in the fourth slice ($z = 0$ cm), which corresponds to the plane containing the two corner reflectors on the large cylindrical support.

In the fifth slice ($z = 6$ cm), the magnitude of the response decreased owing to the mismatch between the heights of the corner reflector and imaging plane. The magnitude of the two peaks decreased as the height of the imaging plane increased, until it diminished in the eighth slice ($z = 24$ cm).

On the other hand, a distinct response at (x, y) coordinates of $(0$ m, 0.3 m$)$ began to appear as a single peak in the seventh slice ($z = 18$ cm). The magnitude of this peak increased as the height of the imaging plane increased, until it reached its maximum value in the ninth slice ($z = 30$ cm). The height of the imaging plane corresponds to that of the smaller cylindrical support, which contains a single corner reflector.

The magnitude of the response from the corner reflector on the smaller cylindrical support decreased with the increasing height from the ninth slice to the final slice. In the twelfth slice ($z = 48$ cm), the responses from all the three corner reflectors diminished. Overall, by analyzing multiple slices of 3-D imaging results with different heights, the individual targets were separated in the volumetric space and the positions of the point scatterers were localized.

To assess the proposed method considering targets with complex scattering, an experiment was performed using a ground vehicle as the illuminated target. The vehicle model was a K3 sedan manufactured by KIA, with most of its body composed of steel. The length, width, and height of the vehicle were 4.6 m, 1.8 m, and 1.4 m, respectively.

The top portion of Fig. 11 depicts an image of the target, which was placed 45 m from the radar hardware in the LOS direction. During the experiment, the vehicle was positioned such that the length was parallel to the along-track direction. Considering the experimental geometry, the x-, y-, and z-axes are overlaid with the target image in Fig. 11.

In Fig. 11 (a), an $x - y$ slice of the 3-D imaging result is depicted on a 3-D projection grid. The position of the slice is $z = -0.55\ m$, which corresponds to a plane parallel to the ground plane and 55 cm below the radar hardware. According to the imaging geometry, the plane intersects with the body of the target vehicle.

The bottom portion Fig. 11 (a) depicts the aforementioned $x - y$ slice for a detailed analysis. As indicated in the figure, a large response exists from $x = -1.1$ m to $x = 3.2$ m. The range of the large response in the x-direction corresponds to the length of the target vehicle. However, large response in the y-direction is visible only from $y = -0.7$ m to $y = -0.3$ m. The range of response in the y-direction limited in comparison with the vehicle width of 1.4 m. This can be attributed to the insufficient height of the radar hardware. As the radar hardware was mounted at a height lower than that of the vehicle, most of the energy was backscattered from the side of the vehicle. Nevertheless, the $x - y$ slice indicates the along-track imaging capability of the proposed method for complex targets.

Fig. 11 (b) illustrates an $x - z$ slice of the imaging result, overlaid with the projection grid depicted in Fig. 11 (a). The position of the slice was $y = -0.74$ m, which was 74 cm closer to the radar in the range direction compared to the scene center. An illustration of the position of the slice is shaded blue on the image of the target vehicle.

The bottom portion of Fig. 11 (b) illustrates the aforementioned $x - z$ slice for a detailed analysis. The figure indicates a large response above $z = 0$ m, which is the response backscattered from the side of the vehicle. Based on the vehicle shape, the height of the vehicle roofline decreased from the middle to the rear of the vehicle body. The response corresponding to the vehicle shape is apparent in Fig. 11 (b) because the height of the large response decrease with the increasing x-values.

Additionally, a large response below $z = 0$ m is apparent near $x = -0.7$ m and $x = 2$ m. The height of the large response is $z = -0.5$ m, which corresponds to the height of the vehicle wheels. The complex metallic structure of the vehicle wheels results in a large response in the image. Overall,

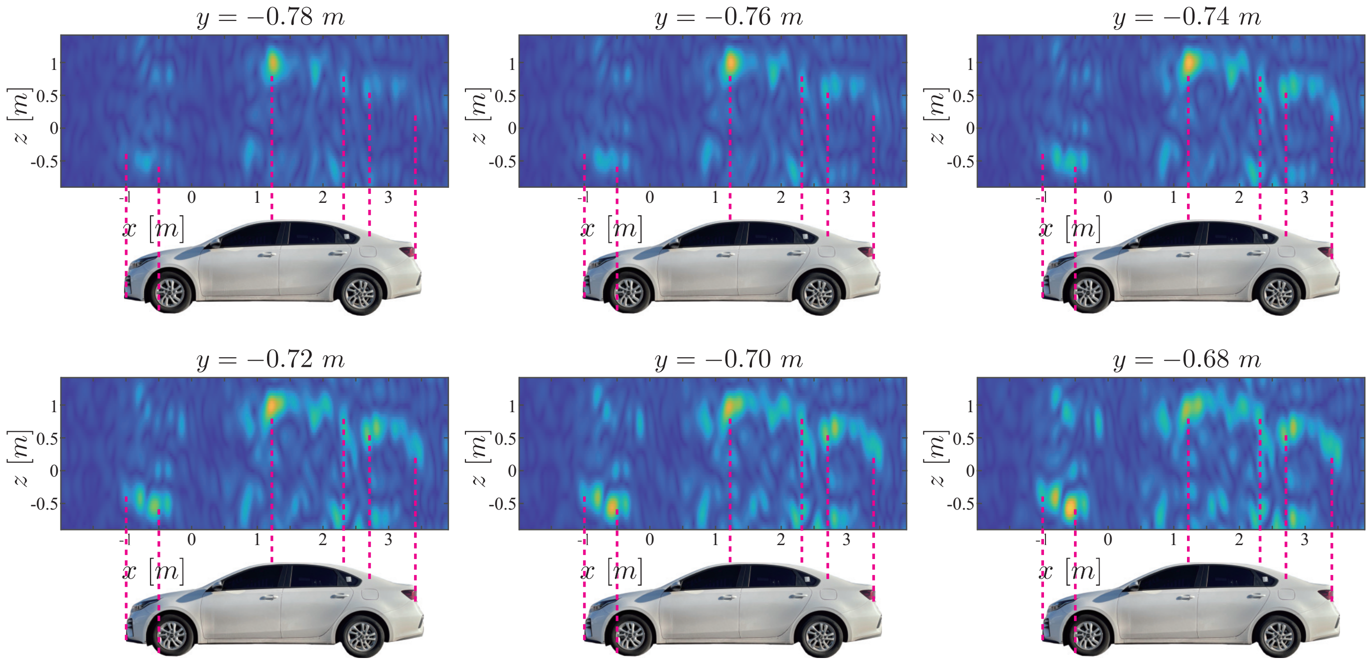

Fig. 12. Six $x - z$ slices of the three-dimensional (3-D) imaging result from $y = -0.78$ m to $y = -0.68$ m.

the silhouette of the ground vehicle in the length and height directions can be identified from the imaging results.

To analyze the imaging result further, six $x - z$ slices of the imaging result from $y = -0.78$ m to $y = -0.68$ m were depicted in Fig. 12. The slices correspond to the planes that were normal to the radar LOS direction. The backscattered information from different ranges can be compared and analyzed by sequentially arranging multiple images. Fig. 12 illustrates the up-to-scale images of the vehicle along with the imaging results.

The location of the first slice ($y = -0.78$ m) corresponds to a plane 78 cm closer to the radar from the scene center. According to the first slice, reflections from the body and roof of the vehicle are dominant.

In the second and third slice ($y = -0.76$ m, $y = -0.74$ m), a large response from the vehicle wheels begins to appear below $z = 0$ m. The location of the imaging plane is 2 cm to 4 cm further in the range direction compared to the first slice. Owing to the complex structure of the wheels, the transmitted signals undergo a larger travel time. The geometric conditions are manifested as reflections from the wheels apparent that appear at further ranges. The magnitude of the response from the wheels increased with with the increasing range. Overall, by analyzing multiple slices of the 3-D imaging results with different ranges, the detailed structure of the ground vehicle can be obtained in the volumetric space can be analyzed.

V. Conclusion

In this study, we proposed a method to synthesize a 3-D microwave image using a MIMO radar and derived an efficient imaging algorithm. MIMO technology can increase the number of channels with reduced hardware, which can be used to to increase the cross-track resolution of a 3-D radar image. By utilizing the BFD FMCW waveform, the MIMO technology can be adopted for 3-D radar imaging without hindering the performance in the along-track direction.

Synthesizing a 3-D image using the massive amount of data acquired from a MIMO radar may be time-consuming. Therefore, the MIMO radar signal is modeled according to the imaging geometry. Furthermore, an imaging algorithm that utilizes the efficient calculation of the FFT is proposed. According to the proposed imaging algorithm, a 3-D radar image can be synthesized from range-compressed MIMO radar data by interpolating the data in the frequency domain and performing Fourier transform.

The proposed imaging method and algorithm were validated by synthesizing a 3-D image from simulated radar data, which was generated by assuming distributed point scatterers distributed in a volumetric space. The amplitude distribution in the 3-D space validates the effectiveness of the proposed imaging method and algorithm.

To validate the proposed method further, the algorithm was applied to the data acquired from an operational W-band MIMO radar. The transceiver, signal processor, power board, and control PC were mounted on a movable platform for data acquisition. Triangular trihedral corner reflectors and a personal vehicle were used as targets for data acquisition. The imaging results obtained using corner reflectors indicated an accurate amplitude distribution, facilitating the localization of point targets in the volumetric space. The imaging results obtained using a personal vehicle verified that the proposed method can be applied to complex artificial targets.

References

[1] S.-Y. Jeon, M.-H. Ka, S. Shin, M. Kim, S. Kim, S. Kim, J. Kim, A. Dewantari, J. Kim, and H. Chung, "W-band mimo fmcw radar system with simultaneous transmission of orthogonal waveforms for high-resolution imaging," *IEEE Transactions on*

Microwave Theory and Techniques, pp. 1–14, 2018. [Online]. Available: https://dx.doi.org/10.1109/tmtt.2018.2867003

[2] S.-Y. Jeon, S. Kim, J. Kim, S. Kim, S. Shin, M. Kim, and M.-H. Ka, "W-band fmcw mimo radar system for high-resolution multimode imaging with time- and frequency-division multiplexing," *IEEE Transactions on Geoscience and Remote Sensing*, vol. 58, no. 7, pp. 5042–5057, 2020. [Online]. Available: https://dx.doi.org/10.1109/tgrs.2020.2971998

[3] J. Li and P. Stoica, "Mimo radar signal processing," 2008.

[4] G. Krieger, "Mimo-sar: Opportunities and pitfalls," *IEEE Transactions on Geoscience and Remote Sensing*, vol. 52, no. 5, pp. 2628–2645, 2014.

[5] M. Soumekh and a. O. M. C. Safari, *Synthetic Aperture Radar Signal Processing with MATLAB Algorithms*. Wiley-Interscience, 1999. [Online]. Available: https://books.google.co.kr/books?id=XTnOzQEACAAJ

[6] J. Curlander and R. McDonough, *Synthetic Aperture Radar: Systems and Signal Processing*, ser. Wiley Series in Remote Sensing and Image Processing. Wiley, 1992. [Online]. Available: https://books.google.co.kr/books?id=nM98QgAACAAJ

[7] C. D. Austin, E. Ertin, and R. L. Moses, "Sparse signal methods for 3-d radar imaging," *IEEE Journal of Selected Topics in Signal Processing*, vol. 5, no. 3, pp. 408–423, 2011. [Online]. Available: https://ieeexplore.ieee.org/document/5613143/

[8] A. Reigber and A. Moreira, "First demonstration of airborne sar tomography using multibaseline l-band data," *IEEE Transactions on Geoscience and Remote Sensing*, vol. 38, no. 5, pp. 2142–2152, 2000. [Online]. Available: https://ieeexplore.ieee.org/document/868873/

[9] Y. Huang, J. Levy-Vehel, L. Ferro-Famil, and A. Reigber, "Three-dimensional imaging of objects concealed below a forest canopy using sar tomography at l-band and wavelet-based sparse estimation," *IEEE Geoscience and Remote Sensing Letters*, vol. 14, no. 9, pp. 1454–1458, 2017. [Online]. Available: https://ieeexplore.ieee.org/document/7990051/

[10] H. Liu, Z. Guo, L. Pang, L. Zhang, F. Li, X. Zhou, and W. Sun, "Spatial shift phenomenon compensation for tomosar imaging using high-resolution terrasar-x data," *IEEE Access*, vol. 9, pp. 13 970–13 980, 2021. [Online]. Available: https://ieeexplore.ieee.org/document/9323037/

[11] F. Zhang, X. Liang, R. Cheng, Y. Wan, L. Chen, and Y. Wu, "Building corner reflection in mimo sar tomography and compressive sensing-based corner reflection suppression," *IEEE Geoscience and Remote Sensing Letters*, vol. 17, no. 3, pp. 446–450, 2020. [Online]. Available: https://ieeexplore.ieee.org/document/8765383/

[12] G. Fornaro and F. Serafino, "Imaging of single and double scatterers in urban areas via sar tomography," *IEEE Transactions on Geoscience and Remote Sensing*, vol. 44, no. 12, pp. 3497–3505, 2006. [Online]. Available: https://ieeexplore.ieee.org/document/4014314/

[13] S. Xing, Y. Li, D. Dai, and X. Wang, "Three-dimensional reconstruction of man-made objects using polarimetric tomographic sar," *IEEE Transactions on Geoscience and Remote Sensing*, vol. 51, no. 6, pp. 3694–3705, 2013. [Online]. Available: https://ieeexplore.ieee.org/document/6375810/

[14] O. Ponce, P. Prats-Iraola, M. Pinheiro, M. Rodriguez-Cassola, R. Scheiber, A. Reigber, and A. Moreira, "Fully polarimetric high-resolution 3-d imaging with circular sar at l-band," *IEEE Transactions on Geoscience and Remote Sensing*, vol. 52, no. 6, pp. 3074–3090, 2014. [Online]. Available: https://dx.doi.org/10.1109/tgrs.2013.2269194

[15] D. Feng, D. An, L. Chen, and X. Huang, "Holographic sar tomography 3-d reconstruction based on iterative adaptive approach and generalized likelihood ratio test," *IEEE Transactions on Geoscience and Remote Sensing*, vol. 59, no. 1, pp. 305–315, 2021. [Online]. Available: https://ieeexplore.ieee.org/document/9099001/

[16] O. Ponce, P. Prats-Iraola, R. Scheiber, A. Reigber, and A. Moreira, "First airborne demonstration of holographic sar tomography with fully polarimetric multicircular acquisitions at l-band," *IEEE Transactions on Geoscience and Remote Sensing*, vol. 54, no. 10, pp. 6170–6196, 2016. [Online]. Available: https://dx.doi.org/10.1109/tgrs.2016.2582959

[17] C. Tsz-King, Y. Kuga, and A. Ishimaru, "Experimental studies on circular sar imaging in clutter using angular correlation function technique," *IEEE Transactions on Geoscience and Remote Sensing*, vol. 37, no. 5, pp. 2192–2197, 1999. [Online]. Available: https://ieeexplore.ieee.org/document/789616/

[18] Y. Lin, W. Hong, W. Tan, Y. Wang, and Y. Wu, "Interferometric circular sar method for three-dimensional imaging," *IEEE Geoscience and Remote Sensing Letters*, vol. 8, no. 6, pp. 1026–1030, 2011. [Online]. Available: https://ieeexplore.ieee.org/document/5875868/

[19] S. Jun, Z. Xiaoling, Y. Jianyu, and W. Chen, "Apc trajectory design for "one-active" linear-array three-dimensional imaging sar," *IEEE Transactions on Geoscience and Remote Sensing*, vol. 48, no. 3, pp. 1470–1486, 2010. [Online]. Available: https://ieeexplore.ieee.org/document/5291764/

[20] L. Kang, T. c. Sun, Y. Luo, Q. Zhang, and J. c. Ni, "Downward-looking linear array three-dimensional sar imaging based on the two-dimensional mismatch compensation," *IEEE Journal of Selected Topics in Applied Earth Observations and Remote Sensing*, vol. 14, pp. 258–269, 2021.

[21] S. Zhang, Y. Zhu, and G. Kuang, "Imaging of downward-looking linear array three-dimensional sar based on fft-music," *IEEE Geoscience and Remote Sensing Letters*, vol. 12, no. 4, pp. 885–889, 2015. [Online]. Available: https://ieeexplore.ieee.org/document/6955795/

[22] X. Peng, W. Hong, Y. Wang, W. Tan, and Y. Wu, "Polar format imaging algorithm with wave-front curvature phase error compensation for airborne dlsla three-dimensional sar," *IEEE Geoscience and Remote Sensing Letters*, vol. 11, no. 6, pp. 1036–1040, 2014. [Online]. Available: https://ieeexplore.ieee.org/document/6680630/

[23] S. Zhang, G. Dong, and G. Kuang, "Superresolution downward-looking linear array three-dimensional sar imaging based on two-dimensional compressive sensing," *IEEE Journal of Selected Topics in Applied Earth Observations and Remote Sensing*, vol. 9, no. 6, pp. 2184–2196, 2016. [Online]. Available: https://ieeexplore.ieee.org/document/7458126/

[24] J.-H. Kim, "Multipe-input multiple-output synthetic aperture radar for multimodal operation," Ph.D. thesis, 2011. [Online]. Available: http://dx.doi.org/10.5445/IR/1000028740

[25] J.-H. Kim, M. Younis, A. Moreira, and W. Wiesbeck, "A novel ofdm chirp waveform scheme for use of multiple transmitters in sar," *IEEE Geoscience and Remote Sensing Letters*, vol. 10, no. 3, pp. 568–572, 2013. [Online]. Available: https://dx.doi.org/10.1109/lgrs.2012.2213577

[26] R. Feger, C. Pfeffer, and A. Stelzer, "A frequency-division mimo fmcw radar system based on delta–sigma modulated transmitters," *IEEE Transactions on Microwave Theory and Techniques*, vol. 62, no. 12, pp. 3572–3581, 2014. [Online]. Available: https://dx.doi.org/10.1109/tmtt.2014.2364220

[27] H. Forsten, T. Kiuru, M. Hirvonen, M. Varonen, and M. Kaynak, "Scalable 60 ghz fmcw frequency-division multiplexing mimo radar," *IEEE Transactions on Microwave Theory and Techniques*, vol. 68, no. 7, pp. 2845–2855, 2020. [Online]. Available: https://dx.doi.org/10.1109/tmtt.2020.2980521

[28] H. J. Ng, R. Hasan, and D. Kissinger, "A scalable four-channel frequency-division multiplexing mimo radar utilizing single-sideband delta–sigma modulation," *IEEE Transactions on Microwave Theory and Techniques*, vol. 67, no. 11, pp. 4578–4590, 2019. [Online]. Available: https://dx.doi.org/10.1109/tmtt.2019.2930499

[29] J. Moll, P. Schops, and V. Krozer, "Towards three-dimensional millimeter-wave radar with the bistatic fast-factorized back-projection algorithm—potential and limitations," *IEEE Transactions on Terahertz Science and Technology*, vol. 2, no. 4, pp. 432–440, 2012. [Online]. Available: https://dx.doi.org/10.1109/tthz.2012.2199113

[30] B. D. Rigling and R. L. Moses, "Polar format algorithm for bistatic sar," *IEEE Transactions on Aerospace and Electronic Systems*, vol. 40, no. 4, pp. 1147–1159, 2004. [Online]. Available: https://dx.doi.org/10.1109/taes.2004.1386870

[31] S. Kim and M.-H. Ka, "Forward-looking electromagnetic wave imaging using a radial scanning multichannel radar," *IEEE Geoscience and Remote Sensing Letters*, vol. 19, pp. 1–5, 2022.

[32] S. Kim, S.-Y. Jeon, J. Kim, U.-M. Lee, S. Shin, Y. Choi, and M.-H. Ka, "Multichannel w-band sar system on a multirotor uav platform with real-time data transmission capabilities," *IEEE Access*, vol. 8, pp. 144 413–144 431, 2020.

[33] M. Richards, *Fundamentals of Radar Signal Processing*, ser. Professional Engineering. McGraw-Hill Education, 2005. [Online]. Available: https://books.google.co.kr/books?id=j91oJ22ldoQC

Sumin Kim received his bachelor's degree in School of Integrated Technology from Yonsei University, Republic of Korea, in 2016. Since 2016 he has been a graduate student at Radar Systems and Wave Sensing Lab, School of Integrated Technology, in Yonsei University, Republic of Korea. He is currently a Ph.D. candidate in the School of Integrated Technology, Yonsei University, Republic of Korea, and is currently involved in projects for bistatic and multistatic SAR. His current interests include high resolution radar, synthetic aperture radar, and real-time radar signal processing.

Jeongbae Kim received his B.S.E. at Yonsei University, Seoul, Republic of Korea in 2017. From 2017, He is in the combined master's and doctor's program at Radar Systems and Wave Sensing Laboratory, School of Integrated Technology, Yonsei University, Republic of Korea. He has been participating in several research programs including small drone-based SAR systems, bistatic and multistatic SAR technology, and virtual radar-scape synthesis. Currently, his main academic interest is toward multi-channel multistatic SAR processing and acceleration of various SAR-related techniques.

Jeongbae Kim received her bachelor's degree in School of Integrated Technology from Yonsei University, Republic of Korea, in 2020. Since 2020 she is in the combined master's and doctor's program at Radar Systems and Wave Sensing Laboratory, School of Integrated Technology, Yonsei University, Republic of Korea. She is currently involved in projects for bistatic and multistatic SAR. Her main academic interest is about synthetic aperture radar, radar signal processing, and multistatic SAR.

Min-Ho Ka (M'06) received his B.S. and M.S. degrees in electronics engineering from Yonsei University, Seoul, South Korea, in 1989 and 1991, respectively, and the Ph.D. degree in radio engineering from the Moscow Power Engineering Institute, Moscow, Russia in 1997. From 1997 to 2000, he was with the Agency for Defense Development, Ministry of Defense, South Korea, for the development of microwave imaging sensors and spaceborne and airborne synthetic aperture radar (SAR). From 2002 to 2010, he was a Professor with Korea Polytech University, Siheung, South Korea, where he was the Head of the Department of the Korea-Russia Industrial Technology Cooperation Centre. He was also a Chairman with the Radar Group, Korean Institute of Electromagnetic Engineering and Science. He is currently an Professor with the Radar Systems and Wave Sensing Laboratory, School of Integrated Technology, Yonsei University. His current research interests include the system design and development of microwave sensors and spaceborne and airborne SAR.